

The Dusty Progenitor Star of the Type II Supernova 2017eaw

Charles D. Kilpatrick^{1*} and Ryan J. Foley¹

¹*Department of Astronomy and Astrophysics, University of California, Santa Cruz, CA 95064, USA*

Accepted 0000, Received 0000, in original form 0000

ABSTRACT

We present pre-explosion photometry of the likely progenitor star of the Type II supernova (SN II) 2017eaw in NGC 6946. We use a *Hubble Space Telescope* (*HST*) image of SN 2017eaw to perform relative astrometry with *HST* and *Spitzer Space Telescope* (*Spitzer*) imaging, finding a single point source consistent with its position. We detect the progenitor star in >40 epochs of *HST* and *Spitzer* imaging covering 12.9 years to 43 days before discovery. While the progenitor luminosity was roughly constant for most of this period, there was a $\sim 20\%$ increase in its $4.5\ \mu\text{m}$ luminosity over the final 3 years before explosion. We interpret the bright mid-infrared emission as a signature of circumstellar dust around the progenitor system. Using the pre-explosion photometry and assuming some circumstellar dust, we find the progenitor is most likely a red supergiant with $\log(L/L_{\odot}) = 4.9$ and $T = 3350\ \text{K}$, obscured by a $> 2 \times 10^{-5}\ M_{\odot}$ dust shell with $R = 4000\ R_{\odot}$ and $T = 960\ \text{K}$. Comparing to single-star evolutionary tracks, we find that the progenitor star had an initial mass of $13\ M_{\odot}$ and a mass-loss rate of $2 \times 10^{-7}\ M_{\odot}\ \text{yr}^{-1}$, consistent with the population of SN II progenitor stars.

Key words: stars: evolution — stars: mass loss — supernovae: general — supernovae: individual (SN 2017eaw)

1 INTRODUCTION

Stars with masses $> 8\ M_{\odot}$ undergo core collapse when their iron cores increase in mass and become unstable. The majority of these stars are the red supergiant (RSG) progenitor stars of Type II supernovae (SNe II). This connection between SNe II and RSGs is robustly predicted through comparison of observed supernova rates to the initial mass function (Smith et al. 2011) and measurements of the progenitor star radii from shock cooling models (Rubin et al. 2016). It is also directly shown through the growing sample of resolved RSG progenitor stars of SNe II (for a review see Smartt 2009).

Detailed analysis of the population of RSG SN II progenitor stars indicates that none of them have luminosities above $\log(L/L_{\odot}) \approx 5.2$ (i.e., with initial masses above $17\ M_{\odot}$; Smartt et al. 2015). This observation is in conflict with the hypothesis that all RSGs result in SNe II and the observed luminosities of Galactic RSGs, which extend up to $\log(L/L_{\odot}) = 5.5\text{--}5.6$ (i.e., with initial masses up to $25\ M_{\odot}$; Levesque et al. 2005; Massey et al. 2009). Assuming a Salpeter initial mass function, roughly 66% of RSG stars with initial masses above $8.5\ M_{\odot}$ ought to have $M_{\text{init}} > 16.5\ M_{\odot}$ (see Smith et al. 2011, for a detailed analysis). However, there are now over 13 robust detections of RSG SN progenitor stars in the literature, none of which fall in this mass range (e.g., SNe 2003gd, 2004A, 2004et, 2005cs, 2006my,

2008bk, 2009hd, 2009kr, 2009md, 2012A, 2012aw, 2012ec, 2016cok; Smartt et al. 2004; Maund & Smartt 2009; Maund 2009; Fraser et al. 2010; Crockett et al. 2011; Elias-Rosa et al. 2011; Fraser et al. 2011; Maund et al. 2013; Tomasella et al. 2013; Fraser et al. 2014; Maund et al. 2014; Kochanek et al. 2017). It is extremely unlikely that all of the observed RSG SN progenitors would have had initial masses $< 17\ M_{\odot}$ assuming they all come from a typical mass function. This apparent conflict is the so-called “red supergiant problem.”

One solution to this problem is that there is in fact a maximum mass for RSG SN progenitor stars above which RSGs do not produce SNe. Smartt (2009) and Smartt et al. (2015) determine statistically that the current RSG SN progenitor star luminosity estimates are consistent with a maximal mass in the range of $16\text{--}21\ M_{\odot}$. Theoretical predictions indicate that some RSGs whose luminosities exceed this limit may instead produce “failed SNe” and direct collapse or fall back to a black hole (Woosley & Heger 2012; Lovegrove & Woosley 2013). These stars would disappear over a short timescale (Kochanek et al. 2008) or produce a low-luminosity, red transient with a weak shock breakout (Piro 2013; Lovegrove & Woosley 2013). Gerke et al. (2015) report a potential example of a “failed SN” in NGC 6946. The pre-explosion counterpart of this event was consistent with a $25\ M_{\odot}$ RSG that increased gradually in luminosity over several hundred days and then promptly disappeared down to deep limits in optical bands (although a $2000\text{--}3000\ L_{\odot}$ infrared source remains; Adams et al. 2017).

* Email: cdkilpat@ucsc.edu

Even if some high-mass RSGs undergo prompt collapse to a black hole without a SN, it is likely that all SN II progenitor stars are dust-obscured to some degree. RSGs form dust in their winds (Verhoelst et al. 2009), and analysis of resolved circumstellar environments around RSGs in the Milky Way indicates that these winds can form compact shells obscuring the underlying star. SNe II exhibit evidence for coronal line emission in early-time spectra (Khazov et al. 2016), narrow, transient lines of hydrogen consistent with a compact shell of circumstellar material that is irradiated by the SN (Bullivant et al. 2018), and excess mid-infrared emission consistent with heated dust in their circumstellar environments (Tinyanont et al. 2016). If high-mass RSGs are significantly dust-obscured in pre-SN imaging, it is possible that their luminosities and initial masses are underpredicted, or even that some of these stars go completely undetected.

Walmswell & Eldridge (2012) found that the current population of RSG SN progenitor stars could be consistent with a maximum initial mass of $21_{-1}^{+2} M_{\odot}$ assuming that all of them were obscured by dust from a RSG-like wind that was previously unaccounted for in analysis of their spectral energy distributions (SEDs). Similarly, Beasor & Davies (2016) and Davies & Beasor (2018) point out that pre-SN RSGs evolve to later spectral types, and so their luminosities are significantly underestimated when pre-explosion photometry is limited and matched to typical RSG SEDs. Analysis of the progenitor star of the SN 2012aw in Kochanek et al. (2012) can account for absorption and scattering by circumstellar material and find a relatively low-mass progenitor star (compared to, e.g., Van Dyk et al. 2012), but analyses where the SED is so well-constrained are rare. In addition, the total mass of circumstellar dust around SN II progenitor systems is partly constrained by radio and X-ray observations (e.g., Chevalier & Fransson 2003; Dwarkadas & Gruszko 2012; Dwarkadas 2014). These studies suggest that there is not enough material to hide a high-mass RSG in some SN II progenitor systems, but this finding emphasizes the role of circumstellar dust in shaping the observed SEDs of SN progenitor stars.

Here we discuss the SN II 2017eaw in NGC 6946. NGC 6946 is a well-studied galaxy and the host of over 10 luminous transients in the past century (e.g., SN 2002hh, 2004et, 2008S; Barlow et al. 2005; Li et al. 2005; Prieto et al. 2008). SN 2017eaw was discovered in NGC 6946 on 14.24 May 2017 by Wiggins (2017). Cheng et al. (2017) spectroscopically identified SN 2017eaw as a SN II on 14.75 May 2017, with broad H α and strong blue continuum emission. Detailed photometric follow up confirmed that SN 2017eaw exhibited a plateau in its light curve (Tsvetkov et al. 2018), consistent with the explosion of a star with an extended hydrogen envelope. van Dyk et al. (2017) identified a potential RSG progenitor star in pre-explosion *HST* imaging, which was consistent with a RSG with $\log(L/L_{\odot}) = 4.9$ and an initial mass of $13 M_{\odot}$. Johnson et al. (2017) used 9 yr of *UBVR* imaging of the site of SN 2017eaw to demonstrate that its progenitor system was not extremely variable in optical bands.

We report detailed analysis of pre-explosion *HST* and *Spitzer* imaging of the site of SN 2017eaw. We identify a single point source consistent with being of the SN 2017eaw progenitor star. This star is detected in multiple epochs of *HST*/ACS and *Spitzer*/IRAC imaging where it exhibits a persistent mid-infrared excess consistent with predictions of a RSG surrounded by a compact circumstellar dust shell. The source decreased by 30% in the *HST*/*F814W* (roughly *I*) band over 12 years and increased by 20% in *Spitzer* 4.5 μm emission around 1000 days before discovery. Following methods used in the analysis of the progenitor star of

SN 2012aw by (Kochanek et al. 2012), we fit a SED of a model RSG to optical to mid-infrared photometry of the SN 2017eaw counterpart from roughly 200 days before core-collapse and determine that it was most likely a $13 M_{\odot}$ star surrounded by a relatively low mass dust shell. Although the SN 2017eaw progenitor star is among the most massive known SN II progenitor stars (compared to examples in Smartt et al. 2015), it is consistent with predictions that the RSG progenitor stars of SN II have an upper limit in mass.

Throughout this paper, we assume a distance to NGC 6946 of 6.72 ± 0.15 Mpc (derived from the tip of the red giant branch (TRGB) by Tikhonov 2014). This value differs somewhat from ≈ 5.6 – 5.8 Mpc derived using SNe II and the Tully-Fisher relation (e.g., see Terry et al. 2002; Sahu et al. 2006; Rodríguez et al. 2014), but the TRGB method is well-calibrated and this distance to NGC 6946 has already been used in the literature (e.g., Murphy et al. 2018; Williams et al. 2018). For the Milky Way extinction to NGC 6946, we take $E(B - V) = 0.30$ mag from Schlafly & Finkbeiner (2011).

2 DATA

2.1 Hubble Space Telescope

We obtained *HST*/ACS and WFC3 imaging of NGC 6946 from the Mikulski Archive for Space Telescopes¹. These data were taken between 29 Jul. 2004 and 26 Oct. 2016 (SNAP-9788, PI Ho; GO-14156, PI Leroy; GO-14638, PI Long; GO-14786, PI Williams). The individual *flc* and *flt* files were processed using the relevant calibration files, including corrections for bias, dark current, flat-fielding, and bad-pixel masking. We combined the individual files from each epoch with *DrizzlePac*, which performs cosmic-ray removal and image combination using the *Drizzle* algorithm. With the drizzled images as a reference, we performed photometry on the individual *flc*/*flt* frames using *dolphot*². We used standard *dolphot* parameters recommended for ACS/WFC and WFC3/IR. The instrumental magnitudes were calibrated using zeropoints from the ACS/WFC zeropoint calculator tool for 29 Jul. 2004 and 26 Oct. 2016³ and using the WFC3/IR photometric zeropoints available at <http://www.stsci.edu/hst/wfc3/analysis/>.

In addition, we obtained a single epoch of *HST*/WFC3 *F814W* imaging of SN 2017eaw obtained on 5 Jan. 2018 (SNAP-15166, PI Filippenko). These images consisted of 2×390 s frames, which we drizzled together using the same process described above and then performed photometry using *dolphot*. SN 2017eaw was easily identified in these images (Figure 1) and had a *F814W* Vega magnitude of 15.290 ± 0.004 mag.

2.2 Spitzer

We obtained *Spitzer*/IRAC exposures of NGC 6946 taken between 12 Sep. 2004 and 31 Mar. 2017 from the *Spitzer* Heritage Archive. The Basic Calibrated Data (*bcd*) files were processed using *MOPEX*, and each epoch was combined into a single frame with a scale of $0''.6 \text{ pixel}^{-1}$. SN 2017eaw was detected in a relatively crowded field and close to a cluster in the northern spiral arm of NGC 6946 (Figure 2). Using methods described in Kilpatrick et al.

¹ <https://archive.stsci.edu/>

² <http://americano.dolphinsim.com/dolphot/>

³ <https://acszeropoints.stsci.edu/>

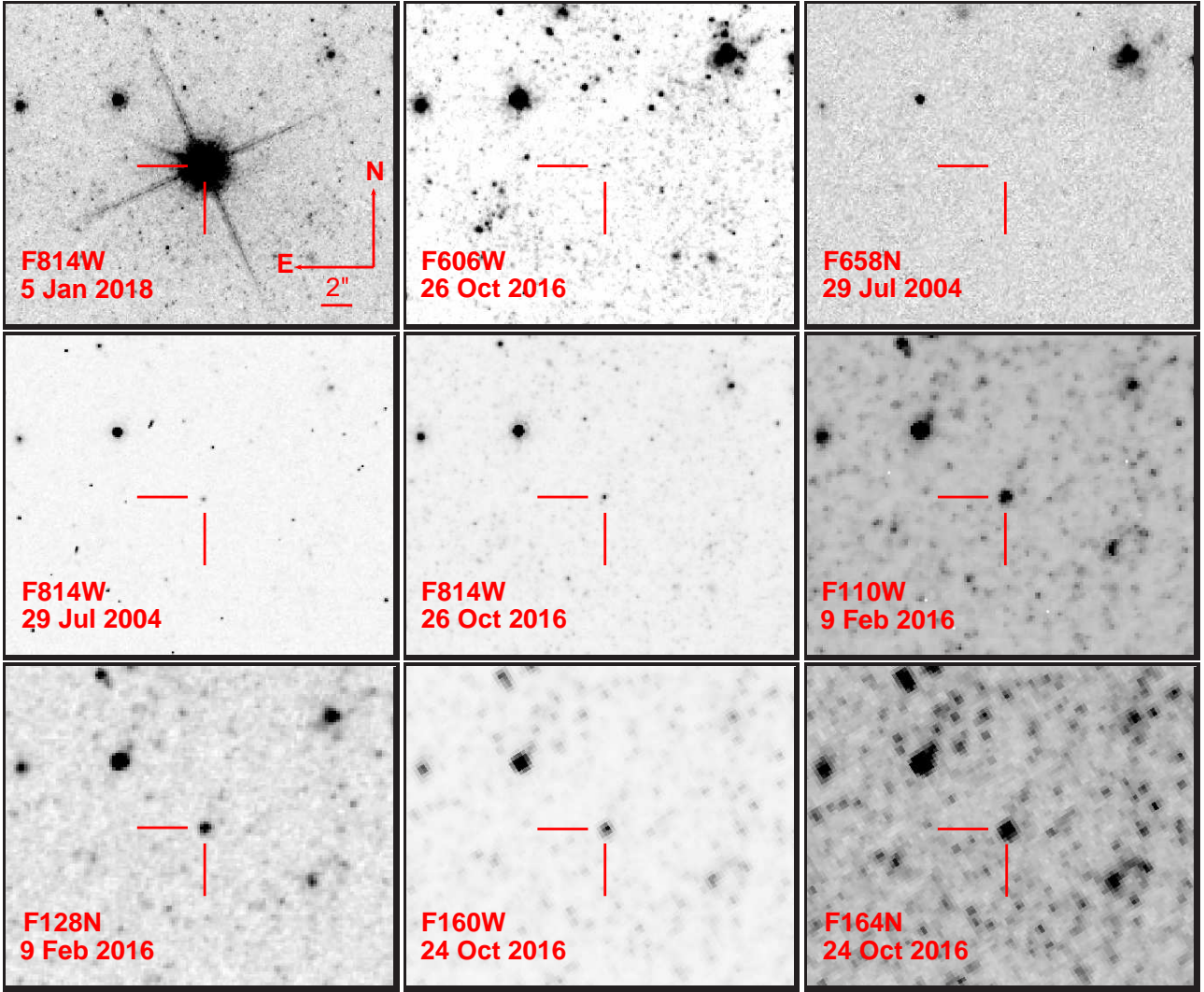


Figure 1. *HST/ACS* and *WFC3* imaging of a $12.3'' \times 10.4''$ region centered on SN 2017eaw (upper left) and the pre-explosion source. The other panels show pre-explosion imaging, with the bandpass and observation date for each image is given in the lower-left the panel. The locations of SN 2017eaw and its pre-explosion counterpart are denoted with red lines in each panel.

(2018), we performed unforced *IRAF/daophot* photometry on all images using a point spread function (PSF) constructed empirically from isolated stars. Each measurement was calibrated using zeropoints given in the *IRAC* instrument handbook for the cold or warm *Spitzer* mission, depending on the epoch of observation⁴. We also calculate 3σ upper limits on the presence of a source at the location of SN 2017eaw by injecting fake stars with the empirical PSF and repeating our *daophot* photometry. We show example epochs for Channels 1 (3 Jul. 2007) and 2 (29 Dec. 2006) centered on the explosion site of SN 2017eaw in Figure 2.

2.3 Spectroscopy

We obtained a low-resolution spectrum of SN 2017eaw with the 2-m Faulkes Telescope North using the FLOYDS spectrograph on 19.52 May 2017. This observation was facilitated by the Las Cumbres Observatory (LCO; Brown et al. 2013) Global Telescope Net-

work (NOAO–17AB, Program 12, PI Kilpatrick). We reduced and extracted the spectrum following standard procedures in *IRAF*. Using arc lamp spectra obtained immediately before the observation, we wavelength-calibrated the spectrum. Finally, we performed flux calibration using a spectrum of the spectrophotometric standard LTT 4364 taken the previous night and in the same instrumental configuration. Our final spectrum is shown in Figure 3.

3 RESULTS

3.1 Spectral Classification of SN 2017eaw

Our spectrum of SN 2017eaw in Figure 3 has been de-reddened for Milky Way extinction and the recessional velocity of NGC 6946 ($z = 0.00133$; Epinat et al. 2008) has been removed. The most notable features are that this spectrum exhibits strong, blue continuum emission with relatively strong $H\alpha$ emission (full-width at half-maximum of $11,000 \text{ km s}^{-1}$). These spectral characteristics indicate that SN 2017eaw was a SN II with a hot, optically thick photosphere similar to young SNe II. Given that we obtained

⁴ <http://irsa.ipac.caltech.edu/data/SPITZER/docs/irac/instrumentation/irac12/instrumentation/irac12.html>

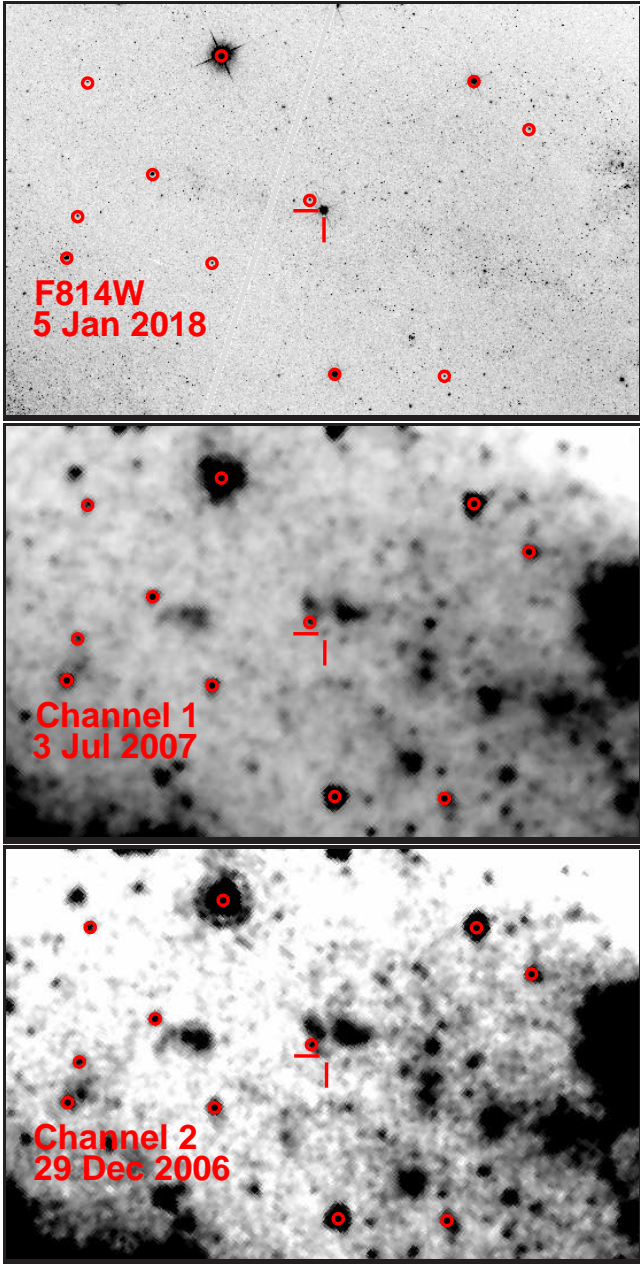


Figure 2. (Top): *HST*/WFC3 *F814W* image from the top-left of [Figure 1](#) showing a $128'' \times 80''$ region with the location of SN 2017eaw denoted with red lines. We circle 10 sources used for relative astrometry with *Spitzer* imaging. (Middle): *Spitzer*/IRAC Channel 1 imaging of NGC 6946 from 3 Jul. 2007. We highlight the location of the pre-explosion mid-infrared counterpart of SN 2017eaw with red lines and circle the same 10 common sources in the top panel. (Bottom): Same as the middle panel, but for *Spitzer*/IRAC Channel 2 imaging from 29 Dec. 2006.

our spectrum 5 days after discovery, SN 2017eaw was likely very young at the time of observation.

We also compare SN 2017eaw to a spectrum of SN 2012aw at around 8 days after discovery (as shown in [Figure 3](#); see also [Dall’Ora et al. 2014](#)). The SN 2012aw spectrum has been de-reddened based on extinction estimates in ([Dall’Ora et al. 2014](#)) and the recessional velocity of its host galaxy has been removed. These two spectra are remarkably similar. The fact that the contin-

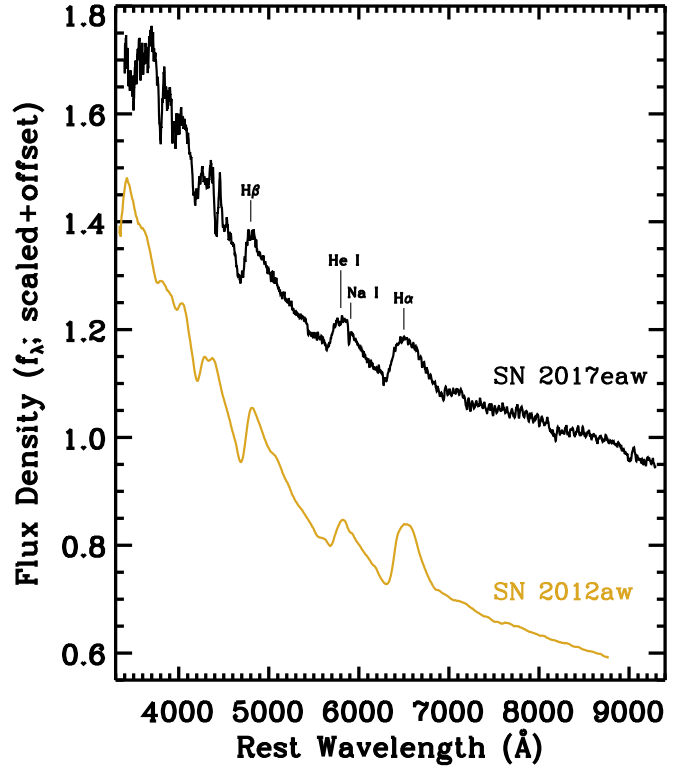


Figure 3. Our Faulkes North/FLOYDS spectrum of SN 2017eaw, which has been de-reddened for Milky Way extinction and the recessional velocity of NGC 6946 has been removed. We note several spectroscopic features in this spectrum. For comparison, we also plot a spectrum of SN 2012aw from [Dall’Ora et al. \(2014\)](#) and obtained 8 days after discovery of this SN. We note the similar continuum shapes and spectroscopic features between both spectra.

uum shapes are similar could suggest that we are fully accounting for Galactic, host, and circumstellar extinction in both objects, and thus that SN 2017eaw has very little host or circumstellar extinction, although this is still very uncertain. There could also be a mismatch between the intrinsic continuum shapes. We must consider other extinction indicators toward SN 2017eaw in order to separate the total extinction contribution from all sources.

NGC 6946 is a face-on spiral galaxy and there is no evidence for background emission or bright sources close to the position of SN 2017eaw that indicate it is embedded in a cluster or dense interstellar gas ([Figure 1](#)). Typically, Na I D absorption in spectra of the SN itself can provide a constraint on the host extinction to the progenitor source. Although strong Na I D absorption is present in our identification spectrum of SN 2017eaw, any host extinction would be blended with Milky Way extinction given our spectral resolution and the redshift to NGC 6946. Therefore, this feature is likely dominated by the strong Milky Way extinction along this line of sight. The equivalent width of the total Na I D feature (which consists of blended Na I D₁+D₂ in the identification spectrum) is $1.6 \pm 0.1 \text{ \AA}$ corresponding to Milky Way reddening of $E(B - V) = 0.34 \pm 0.05 \text{ mag}$ assuming the relationship in [Poznanski et al. \(2012\)](#). We assume this value for the total Milky Way and host reddening to SN 2017eaw and its progenitor system. We also note that the Milky Way reddening to NGC 6946 is consistent with the lower limit of the value from Na I D, implying that there could be effectively no host reddening.

Table 1. *HST* Photometry of the SN 2017eaw Counterpart

Epoch ^a	Instrument	Filter	Exp. Time (s)	Magnitude (1σ)
−4671.21	ACS/WFC	<i>F</i> 814 <i>W</i>	120	22.550 (036)
−4671.20	ACS/WFC	<i>F</i> 658 <i>N</i>	700	>23.6
−459.48	WFC3/IR	<i>F</i> 128 <i>N</i>	2823.48	19.771 (032)
−459.41	WFC3/IR	<i>F</i> 110 <i>W</i>	455.88	20.712 (012)
−201.60	WFC3/IR	<i>F</i> 160 <i>W</i>	396.92	19.377 (007)
−201.60	WFC3/IR	<i>F</i> 164 <i>N</i>	2396.93	19.109 (012)
−199.50	ACS/WFC	<i>F</i> 606 <i>W</i>	2430	26.366 (049)
−199.43	ACS/WFC	<i>F</i> 814 <i>W</i>	2570	22.825 (009)

^a From discovery on 14.24 May 2017.

3.2 Astrometry Between SN 2017eaw and Pre-Explosion Imaging

We performed relative astrometry between the post-explosion *HST*/WFC3 image and the drizzled pre-explosion *HST*/ACS and WFC3 images. For each pre-explosion frame, we identified 99–700 sources common to both the SN 2017eaw and pre-explosion image. We then calculated and applied a WCS solution to the pre-explosion *HST* image using the IRAF tasks `ccmap` and `ccsetwcs`. We estimated the astrometric uncertainty of the new geometric projection in the pre-explosion *HST* images by selecting random subsamples consisting of half of our common stars, re-calculating the geometric projection, and then determining the offsets between the remaining common stars. In this way, the astrometric uncertainty was generally $\sigma = 0.002\text{--}0.003''$ (0.05–0.075 *HST*/WFC3 pixels) in right ascension and declination.

We determined the position of SN 2017eaw in the post-explosion *HST*/WFC3 *F*814 image to be $\alpha = 20^{\text{h}}34^{\text{m}}44^{\text{s}}.272$, $\delta = +60^{\circ}11'36''.008$, which agrees with a single, unblended point source in all of the *HST* images apart from ACS/*F*658*N* where we do not detect any counterpart at $> 3\sigma$. There are no other detected point sources near the SN position and the background level is flat in this area indicating negligible contamination from faint coincident stars. The PSF parameters are also consistent with a point source. The uncertainty on the position of this source is negligible, and so the total astrometric uncertainty is dominated by uncertainties in relative astrometry. In each *HST*/WFC3 and ACS image, we do not detect any other point sources within a minimum of $0.176''$ ($>50\sigma$) of the location of the counterpart. Therefore, we consider the detected sources to be a viable pre-explosion counterpart to SN 2017eaw. We report the *HST* photometry for this source in Table 1.

We estimate the probability of a chance coincidence in the *HST* images by noting that there are roughly 4,000–8,000 point sources with $S/N > 3$ within a $20''$ radius of the location of SN 2017eaw in each image. The 3σ uncertainty ellipse for the *HST* reference image has a solid angle of $\sim 2.5 \times 10^{-4}$ arcsec², which implies that 0.16% of the region within $20''$ of SN 2017eaw is similarly close (within 3σ) to any point source. This value is roughly the probability of a source aligning with the position of SN 2017eaw by chance.

The source appears to have decreased in *F*814*W* luminosity by 30% from 12.7 to 0.6 yr before core collapse. This is a significant change of 7.8σ , implying significant variability in the SED of this source before SN 2017eaw underwent core-collapse.

We also performed relative astrometry between the

HST/WFC3 image of SN 2017eaw and *Spitzer*/IRAC photometry in order to determine whether there was any mid-infrared source consistent with being the progenitor system of SN 2017eaw. Because the point source full-width at half-maximum (FWHM) is much larger and the signal-to-noise per source is much lower in the *Spitzer*/IRAC images relative to the *HST* images, there were significantly fewer sources to anchor *Spitzer*/IRAC to the *HST* image of SN 2017eaw. In each image, we typically used 7–15 point sources to calculate an astrometric solution. The astrometric uncertainties in the *Spitzer*/IRAC solutions were typically $\sigma = 0.24$ pixels, or $0.144''$ in both directions. In Figure 2, we show example *Spitzer*/IRAC images in Channels 1 and 2 along with the *HST*/WFC3 image of SN 2017eaw. The 10 sources used for relative astrometry are circled in red in each image, which correspond to the `daophot` positions in the *Spitzer*/IRAC images and `dolphot` positions in the *HST* image.

In each *Spitzer*/IRAC image, there is at most one point source consistent with being the progenitor star of SN 2017eaw. No other *HST* sources are coincident with the *Spitzer* source. The position of this source agrees with the *HST* position to within the 1σ uncertainties and the closest point source identified in any image is $3.4''$ (23.6σ) away from this source. Following the method outlined above for *HST* imaging, we estimate the chance coincidence in *Spitzer*/IRAC imaging within a $20''$ radius of this source to be 2.3% or smaller per image. Thus, it is unlikely that this source is a chance coincidence and is therefore likely to be the mid-infrared pre-explosion counterpart to SN 2017eaw. We detect this source in every Channel 1 and 2 image for which we have data but not in any of the Channel 3 or 4 images, where we place upper limits on the flux density of any such source. We report all detections and upper limits in Table 2.

3.3 Mid-Infrared Light Curves of the Progenitor System

In Figure 4, we plot the *Spitzer*/IRAC Channels 1 and 2 (3.6 and $4.5\mu\text{m}$) light curves of the SN 2017eaw counterpart. The light curve indicates that the mid-infrared source was persistent for over ~ 13 yr prior to core collapse. The median and standard deviation of the total *Spitzer* light curves are 16.7 and $1.5\mu\text{Jy}$ at $3.6\mu\text{m}$ and 11.4 and $1.6\mu\text{Jy}$ at $4.5\mu\text{m}$. At $3.6\mu\text{m}$, 96% of the data are within 1σ of the median and 100% are within 2σ , which indicates that the data are consistent with measurements of a single value with standard errors and thus exhibited no variability.

At the same time, only 64% of the $4.5\mu\text{m}$ data are within 1σ of the median while 76% are within 2σ . Statistically, this finding indicates that there is likely some variability in this waveband. Combined with the apparent lack of variability at $3.6\mu\text{m}$, the source appears to be changing both in overall mid-infrared color and luminosity. This change is qualitatively apparent in the light curve from Figure 4, where it appears to increase in $4.5\mu\text{m}$ luminosity 1200–500 days before discovery of SN 2017eaw. At the same time, the ratio of $3.6\mu\text{m}$ to $4.5\mu\text{m}$ emission decreases (i.e., the source becomes redder/cooler).

There may still be variability over relatively short timescales. Within the uncertainties of each mid-infrared epoch, the only significant change we detect is the general increase in $4.5\mu\text{m}$ flux from 1200–200 days before discovery. The data in this span of time probe timescales as short as 6 days, which implies that within our photometric precision, there were no significant changes on these timescales. However, our uncertainties are typically $\sim 10\%$ the value of each measurement, and so we are not sensitive to variability comparable to or smaller than this scale.

Table 2. *Spitzer* Photometry of the SN 2017eaw Counterpart

Epoch ^a	Channel 1 (μJy)	Channel 2 (μJy)	Channel 3 (μJy)	Channel 4 (μJy)
-4719.98	17.7 \pm 3.8	11.0 \pm 1.3	<23.5	<67.8
-4626.45	18.6 \pm 3.5	11.1 \pm 1.3	<19.1	<62.1
-4552.00	17.7 \pm 3.8	11.4 \pm 1.1	<30.0	<77.6
-4315.51	17.1 \pm 3.6	10.1 \pm 1.5	<27.9	<64.8
-4151.85	—	—	—	<86.8
-3927.24	—	—	<29.8	—
-3820.83	—	12.5 \pm 1.6	—	<75.5
-3788.71	—	11.9 \pm 2.7	—	<82.7
-3601.77	17.9 \pm 3.8	—	—	—
-3425.67	—	10.6 \pm 1.5	—	<80.8
-3393.89	—	8.6 \pm 1.7	—	<107.4
-3220.95	14.9 \pm 3.4	—	<86.8	—
-2837.75	14.7 \pm 2.0	—	—	—
-2685.13	—	10.1 \pm 0.8	—	—
-2465.17	12.6 \pm 2.0	—	—	—
-2116.88	16.4 \pm 3.9	—	—	—
-2111.92	17.6 \pm 2.1	—	—	—
-1928.68	—	9.9 \pm 0.9	—	—
-1365.60	19.8 \pm 2.1	—	—	—
-1226.16	—	9.3 \pm 1.6	—	—
-1181.13	—	9.4 \pm 0.8	—	—
-1144.19	15.2 \pm 2.0	11.2 \pm 0.9	—	—
-970.55	16.7 \pm 1.9	11.9 \pm 0.9	—	—
-941.18	16.7 \pm 2.0	11.0 \pm 0.8	—	—
-832.76	—	10.9 \pm 1.6	—	—
-619.49	15.8 \pm 2.0	13.4 \pm 0.9	—	—
-613.84	16.7 \pm 1.9	12.3 \pm 0.8	—	—
-604.85	16.4 \pm 2.1	12.4 \pm 0.8	—	—
-592.75	15.5 \pm 1.9	13.4 \pm 0.7	—	—
-535.30	17.5 \pm 1.8	14.4 \pm 0.7	—	—
-506.86	16.5 \pm 1.9	13.7 \pm 0.8	—	—
-213.44	16.6 \pm 1.9	13.9 \pm 0.8	—	—
-134.31	17.7 \pm 1.9	12.9 \pm 0.8	—	—
-42.76	17.9 \pm 2.0	13.4 \pm 0.9	—	—

^a From discovery on 14.24 May 2017.

This trend suggests that in the mid-infrared, the source was variable within ~ 4 yr of core-collapse. If the underlying source is a RSG with a dusty wind (similar to Galactic analogs; [Massey et al. 2005](#)), then it is likely that the $4.5\mu\text{m}$ behavior was driven by dust production. Perhaps this system had an enhanced mass-loss episode leading to a higher density of dust in its circumstellar environment. The mid-infrared emission would have become more optically thick and cooler on a relatively short timescale as the infrared SED shifted to longer wavelengths. This hypothesis is in agreement with the decrease in optical luminosity inferred from *F814W*.

However, the exact nature of the underlying source powering this dust production is less clear from the *Spitzer* light curve. It is possible that the associated optical emission from this source would also have been variable as the RSG underwent an enhanced mass-loss episode. Isolating the SED at a specific epoch in time is essential to determine the intrinsic luminosity of the SN 2017eaw progenitor star, and thus determine its initial mass.

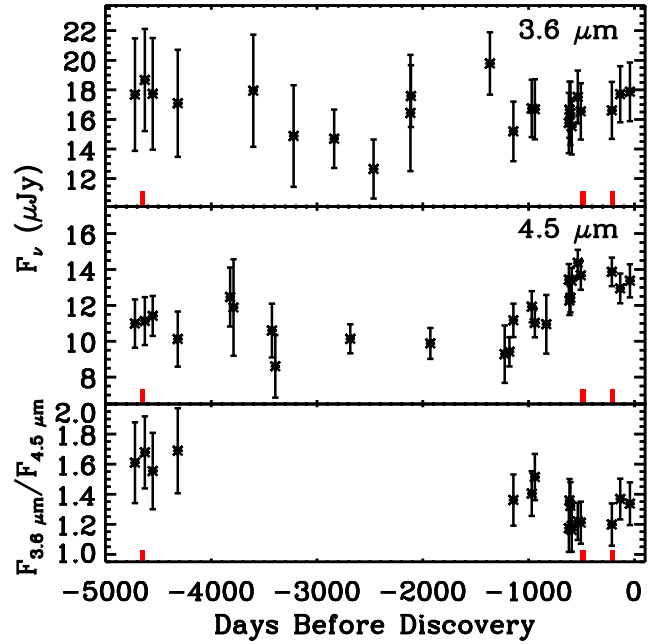


Figure 4. Full $3.6\mu\text{m}$ (*Upper*) and $4.5\mu\text{m}$ (*Middle*) light curves of the SN 2017eaw counterpart. The source does not appear to be significantly variable at $3.6\mu\text{m}$, but it exhibits a notable rise in $4.5\mu\text{m}$ emission starting around 1000 days before the discovery. We also plot the ratio of the emission in the two *Spitzer* bands where they are contemporaneous. The source is significantly brighter in $4.5\mu\text{m}$ emission relative to $3.6\mu\text{m}$ (i.e., redder/cooler) during the last several years before core-collapse relative to ~ 12 yr before core-collapse. We note the three epochs of contemporaneous *HST* imaging using red bars in each panel.

3.4 Evolution of the Spectral Energy Distribution of the Pre-Explosion Source

Under the assumption that the pre-explosion source is mostly dominated by thermal emission from a dust shell or stellar photosphere, we track the evolution of that source over three epochs for which we have *HST* and *Spitzer* data to analyze the optical-infrared variability of that source. These epochs correspond to 29 Jul 2004 to 11 Sep 2004, 23 Dec 2015 to 9 Sep 2016, and 12 Oct 2016 to 26 Oct 2016 (roughly 12.7, 1.3, and 0.6 yr before discovery or core-collapse, respectively). Our fits to the overall SED in these three epochs is shown in [Figure 5](#). For simplicity, we fit blackbody emission (i.e., with emission efficiency $Q = 1$ at all wavelengths).

The best-fitting SED is a thermal source with $\log(L/L_{\odot}) = 4.61 \pm 0.21$, 4.70 ± 0.24 , and 4.80 ± 0.24 and $T = 2540 \pm 160$ K, 2360 ± 200 K, and 2070 ± 220 K in the three epochs, respectively. These values correspond to a photospheric radius of 1000, 1300, and $2000 R_{\odot}$. Overall, these fits suggest the underlying source is cooling and its photosphere is expanding with time, although the luminosity is consistent with being constant.

The simple blackbody model is only a relatively good fit to the full optical to mid-infrared SED in the first epoch of data, which is also where the predicted temperature is hottest and photospheric radius is smallest. Indeed, $1000 R_{\odot}$ is comparable to the radius of many 15–16 M_{\odot} RSGs (based on fits to Mesa Isochrone & Stellar Tracks (MIST) models; [Paxton et al. 2011, 2013, 2015](#); [Dotter 2016](#); [Choi et al. 2016](#))⁵.

⁵ <http://waps.cfa.harvard.edu/MIST/>

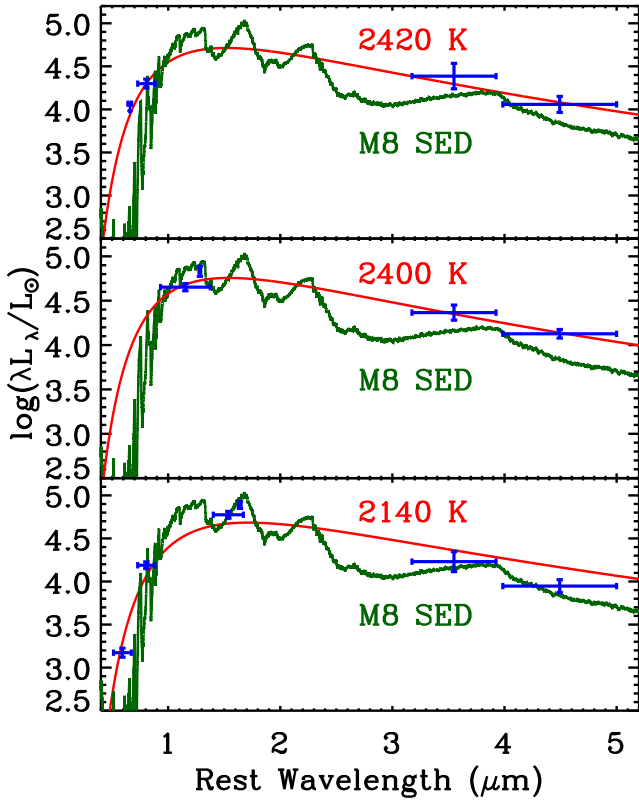


Figure 5. The optical-infrared spectral energy distribution of the SN 2017eaw counterpart over three epochs (blue points; earliest to latest from top to bottom) for which we have *HST* coverage. The data are corrected for Milky Way reddening, shifted to the rest-frame of NGC 6946, and shifted to the assumed distance to SN 2017eaw. We fit the SED in each epoch with a pure blackbody profile (red) with no additional source of extinction or emissivity and note the temperature of the profile in each panel. Under the assumption that this source is an extremely cool supergiant with little or no excess mid-infrared emission, we also fit the SED to a M8 star (green) based on a MARCS photospheric model (Gustafsson et al. 2008).

Suppose that we are seeing the photosphere of a single, ultra-cool supergiant. Detailed analysis of the SEDs and TiO bands observed from Galactic RSGs indicates that the coolest intrinsic temperatures are ≈ 3450 K (for M5 I stars; see, e.g., Levesque et al. 2005). Even if the pre-explosion source were an anomalously cool supergiant with a photosphere approaching an unprecedented value of 2600 K, model photospheres (e.g., from MARCS Gustafsson et al. 2008) with those temperatures fail to simultaneously reproduce the observed optical and mid-infrared photometry (see M8 I fits in Figure 5). The SED is either too bright in the mid-infrared, suggesting some excess source of cool emission (e.g., dust), or too bright in the optical suggesting that we are in fact seeing a hotter photosphere (e.g., from a warmer star). It is more likely that the intrinsic SED has two components consisting of an optical stellar component reddened by circumstellar material and a mid-infrared component from reprocessed emission.

Under the assumption that the SED is dominated by reddened optical emission and mid-infrared dust emission, this would seem to point to a relatively cool star, such as a RSG with a slow, dusty wind that is reddening the intrinsic SED. Overall, the SED is similar to Galactic RSGs, whose SEDs peak around 1.3–1.6 μm and exhibit spectroscopic signatures of infrared dust emission (Verhoelst et al. 2009). However, we must consider the possi-

bility that the intrinsic SED of the pre-explosion counterpart is a significantly hotter source (e.g., a yellow or blue supergiant) that is even more heavily reddened. Below, we perform a physically-motivated analysis of the SED assuming it represents a star with an arbitrary temperature with circumstellar extinction and dust emission.

3.5 Detailed Stellar SED and Dust Models

The optical through mid-infrared SED of the SN 2017eaw progenitor star spanning 214–200 days before discovery of the SN offers an unprecedented opportunity to explore the exact spectral type and characteristics of a SN II progenitor star within the final months before core-collapse. Therefore, we restrict our analysis below to only the *HST*/WFC3 data from Julian Date 2457685.64–2457687.81 and the *Spitzer*/IRAC data from 2457673.81 (i.e., plotted in the bottom panel of Figure 5). These data provide a “snapshot” of the optical to mid-infrared SED of the SN progenitor star over a very narrow window of time and minimise any systematic uncertainties associated with pre-SN variability on timescales longer than 14 days.

As we discuss in Section 3.3, we are not sensitive to mid-infrared variability on scales $\sim 10\%$ or smaller. Moreover, we have no constraint on optical or near-infrared variability apart from the 30% decrease in *F814W* flux over roughly 12 yr. We cannot rule out the possibility that the SN 2017eaw progenitor system is somewhat variable over these 14 days, and so we increase our overall uncertainties by a factor of 2 for the following analysis.

In order to fit these data and investigate the exact SED of the progenitor star, we followed a procedure similar to Kochanek et al. (2012), who analyzed the SED of the progenitor star of SN 2012aw. We began with SEDs derived from MARCS 15 M_{\odot} RSG models of standard composition and spherical geometry (for full descriptions of MARCS models, see Gustafsson et al. 2008). We considered only models at the metallicity of NGC 6946 and with a turbulence parameter of 5 km s^{-1} . Otherwise, we investigated every available MARCS model at a fixed mass, chemical class, geometry, metallicity, and turbulence parameter, but with the full range of available surface gravities ($\log g = -0.5$ to 1.0 in steps of 0.5) and surface temperatures ($T = 2500$ – 4000 K in steps of 100 K as well as 4250 K and 4500 K). In order to expand the range of temperatures in our analysis, we supplemented this set of models with models of hotter (5000–8000 K in steps of 1000 K) and cooler (2600–3200 K in steps of 200 K) photospheres with the same chemical class, geometry, metallicity, and turbulence parameter, but based on a 5 M_{\odot} model and with a range of surface gravities.

To reduce the computational complexity of our analysis, we smoothed each SED of each MARCS model by a factor of 13 from the default resolution of $\lambda/\Delta\lambda = 20,000$ to ≈ 1540 . As in Kochanek et al. (2012), we linearly interpolated between models with different temperatures in order to fit intermediate temperature values. Otherwise, we restricted our analysis to only photospheres with temperatures between 2600 and 8000 K.

To account for optical and infrared extinction due to a shell of dust, we applied a circumstellar extinction law to each MARCS SED, which was calculated from DUSTY models by Kochanek et al. (2012). We repeated our fitting process for four different types of circumstellar extinction (graphitic/silicate dust grains and $R_{out}/R_{in} = 2$ and 10, where R_{out} and R_{in} are the outer and inner radii of the dust shell) and the four different values of $\log g$ without parameterizing over these quantities (i.e., we tested the fit 16 times for all combinations of these dust types and

surface gravities). In general, we found the best fits using graphitic models with $R_{out}/R_{in} = 2$ and stellar SEDs with $\log g = 1.0$.

We tested our fits by comparing the specific luminosity (L_λ) of SN 2017eaw counterpart in each filter, that is the observed flux density (f_λ) corrected for the total Milky Way and host extinction extinction from above ($A_{MW+H,\lambda}$) and at the distance of NGC 6946 (d) such that $L_\lambda = 4\pi d^2 f_\lambda 10^{0.4 \times A_{MW+H,\lambda}}$. We compared these values to the modeled SED $L_{o,\lambda}$ convolved through each *HST* and *Spitzer* filter transmission function. This model SED is calculated as

$$L_{o,\lambda} = \frac{\int_0^\infty \lambda R_\lambda (L_{*,\lambda} 10^{-0.4 \times A_\lambda(\tau_V)} + L_{d,\lambda}) d\lambda}{\int_0^\infty \lambda R_\lambda d\lambda}. \quad (1)$$

Here, $L_{*,\lambda}$ is the scaled, interpolated MARCS model for a certain temperature and surface gravity, $A_\lambda(\tau_V)$ is the total extinction due to dust calculated from the optical depth of the dust shell in *V*-band (τ_V) and for each wavelength of the MARCS SED λ using Table 3 in [Kochanek et al. \(2012\)](#), $L_{d,\lambda}$ is the total luminosity due to dust emission, and R_λ is the filter transmission function.

The dust emission is reprocessed optical light from the obscured star, which illuminates and heats the dust. Therefore, the total dust luminosity is dependent on the luminosity of the underlying star as well as the fraction of that light that is absorbed by the dust (i.e., it is related to A_λ). Here, we parameterize the fraction of the total luminosity that is absorbed by dust as

$$f = \frac{\int_0^\infty (L_{*,\lambda} - L_{*,\lambda} 10^{-0.4 A_\lambda}) d\lambda}{\int_0^\infty L_{*,\lambda} d\lambda}. \quad (2)$$

Thus, the total dust luminosity is related to the intrinsic luminosity of the star as $L_d = f L_*$.

Following analysis in [Kilpatrick et al. \(2018\)](#) (see also [Fox et al. 2010, 2011](#)), we assume the infrared dust emission is optically thin. Therefore, $L_{d,\lambda} = L_0 B_\lambda(T_d) \kappa_\lambda$ where $B_\lambda(T_d)$ is the wavelength-dependent Planck function for a dust temperature T_d and L_0 is a normalization constant such that $\int_0^\infty L_{d,\lambda} d\lambda = L_d$ as described above. We take κ_λ from fig. 4 of [Fox et al. \(2010\)](#) for dust grains with diameter $0.01 \mu\text{m}$, which is roughly consistent with the weighted-average ($\approx 0.0083 \mu\text{m}$) of the [Mathis et al. \(1977\)](#) power-law grain size distribution used in [Kochanek et al. \(2012\)](#). Furthermore, as [Fox et al. \(2010\)](#) note, below $1 \mu\text{m}$ the dust grain size has very little effect on the infrared opacities.

Thus, the full model is parameterized over the total luminosity of the star ($L_* = \int_0^\infty L_{*,\lambda} d\lambda$), the temperature of the interpolated MARCS model (T_*), the optical depth of the dust in *V*-band (τ_V), and the temperature of the dust (T_d). We fit these four parameters to the six *HST*/ACS and *Spitzer*/IRAC specific luminosities from the bottom panel of [Figure 5](#) (i.e., with two degrees of freedom) using a Monte Carlo Markov Chain (MCMC) method by minimising $\chi^2 = (L_\lambda - L_{o,\lambda})^2 / (\sigma_{L_\lambda})^2$ summed over each data point. Here, σ_{L_λ} is the uncertainty for specific luminosity in each filter (including the uncertainties quoted above for photometry and Milky Way extinction). Although we account for distance uncertainty in our final stellar luminosity, the other parameters have no dependence on distance (we simply scaled the input flux densities by our preferred distance), and so we did not include distance uncertainty in our MCMC.

Our best-fitting model to the specific luminosities is shown in [Figure 6](#). The MCMC converged with a final $\chi^2/\text{dof} = 1.5$. We estimated our uncertainties by varying each parameter while fixing the other three to their best-fitting values and determining where

χ^2/dof increased by 2.3 (i.e., the 68% confidence interval for a χ^2 distribution with 2 degrees of freedom). The luminosity is robustly predicted to be $\log(L/L_\odot) = 4.9 \pm 0.2$ regardless of the intrinsic stellar type or dust properties, which is consistent with the simple blackbody fits above.

There is significant degeneracy between τ_V and the stellar temperature (see [Figure 6](#); also discussed in [Kochanek et al. 2012](#); [Fraser et al. 2012](#)). Models with hotter temperatures can produce good fits to the observed data if the circumstellar extinction is higher. This degeneracy can lead to tight or loose constraints on the temperature and circumstellar extinction, although these constraints have systematic uncertainties that are specific to the circumstellar extinction model. We show the full range of this degeneracy (within the formal 1σ uncertainties) for our best-fitting circumstellar extinction (in $A_V \approx 0.79\tau_V$ as in [Kochanek et al. 2012](#)) and stellar temperature. To a lesser extent, the dust temperature is also degenerate with these quantities; in cases where the stellar temperature is low, the dust shell is relatively low luminosity and cool, and it is luminous and hot for a hot star.

These constraints imply a relatively cool best-fitting stellar temperature of $T_* = 3350_{-250}^{+450}$ K, *V*-band optical depth of $\tau_V = 1.6_{-1.2}^{+3.3}$, and a dust temperature of $T_d = 950_{-400}^{+450}$ K. The implied dust luminosity varies from $\log(L_d/L_\odot) = 4.1_{-0.4}^{+0.3}$ with a radius $R_{in} = 4000_{-1300}^{+4000} R_\odot$. The radius of this dust shell is approximately 5 times the photospheric radius of the best-fitting stellar model.

3.6 Physical Properties of the RSG and Circumstellar Material

We compared the total luminosity and temperature of the model star to evolutionary tracks from MIST. Examining only MIST tracks at Solar metallicity and with rotation velocity $v_{rot}/v_{crit} = 0.4$, we find the best fits to evolutionary tracks with initial masses $13_{-2}^{+4} M_\odot$ ([Figure 7](#)).

At the same time, τ_V can be used to constrain the mass of circumstellar material. Using equation (2) in [Kochanek et al. \(2012\)](#), we assume a total mass in the dusty wind of $M = 4\pi\tau_V\kappa_V^{-1}R_{out}R_{in}$ and a mass-loss rate $\dot{M} = 4\pi\tau_V\kappa_V^{-1}v_w R_{in}$. We assume a wind velocity $v_w \approx 10 \text{ km s}^{-1}$ and we derive our visual opacity κ_V from the above dust model.

For the circumstellar material around SN 2017eaw, we find that the total dust mass at the epoch 200 days before core-collapse is $(2 \pm 0.5) \times 10^{-5} M_\odot$ and the mass-loss rate is $9 \times 10^{-7} M_\odot \text{ yr}^{-1}$. The former quantity assumes $R_{out}/R_{in} = 2$, although the outer radius of the dust shell is poorly constrained by our model (we tested only two possible geometries in [Section 3.5](#)), and it could reasonably be much larger than $2 \times R_{in}$. Thus, we consider this dust mass to be a lower limit on the total mass of material.

The mass-loss rate we derive precisely follows the de Jager rate for a star at the derived luminosity of $\log L = 4.9$ ([Woodhams 1993](#); [Huggins et al. 1994](#); [Reimers et al. 2008](#); [Mauron & Josselin 2011](#); [Braun et al. 2012](#)). However, the wind velocity is completely unconstrained by our data and could be a few times larger (e.g., 30–50 km s^{-1} , which is the wind velocity for high-luminosity RSGs such as VY CMa or NML Cyg; [Knapp et al. 1982](#); [Decin et al. 2006](#)). Detailed observations of SN 2017eaw will be necessary to better constrain this parameter.

However, detailed hydrodynamic and pan-chromatic studies of mass loss in RSGs demonstrate that many stars lie below the de Jager prescription depending on the mass-loss tracer and the assumed level of clumping and metallicity ([Mauron & Josselin](#)

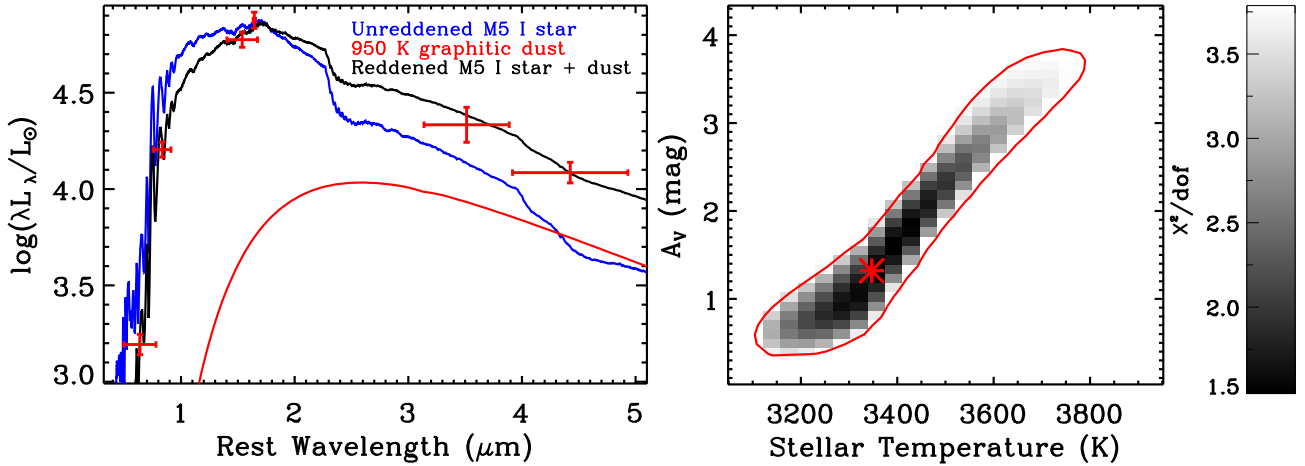


Figure 6. (Left) The optical-infrared SED of the SN 2017eaw counterpart from Julian Date 2457685.64–2457687.81. The data are corrected for Milky Way reddening, shifted to the rest-frame of NGC 6946, and shifted to the assumed distance to SN 2017eaw. We fit the SED in each epoch with a MARCS RSG model (blue curve) that is reddened according to the circumstellar extinction law from Kochanek et al. (2012). We combine this SED with $0.01 \mu\text{m}$ graphitic dust (red curve). The total SED, which is convolved with the relevant *HST* and *Spitzer* filter functions and fit to the observed data, is shown as a black curve. (Right) χ^2/dof parameter estimate of the intrinsic stellar temperature and extinction due to circumstellar material (in $A_V = 0.79\tau_V$ for graphite as in Kochanek et al. 2012). The red star marks the best-fitting parameters while the red line marks the full 1σ uncertainty range (i.e., $\chi^2/\text{dof} = \chi^2_{\text{min}}/\text{dof} + 2.3$). There is a large degeneracy between these two values, although we can reasonably constrain the stellar temperature between 3100 and 3800 K.

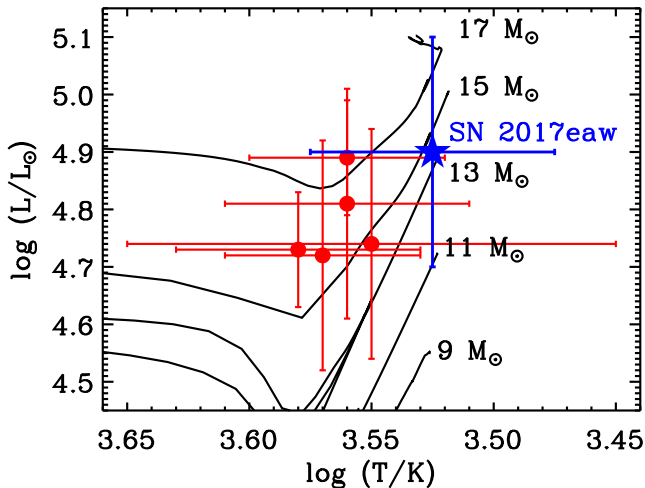


Figure 7. A Hertzsprung-Russell diagram showing the location of our best-fitting model to the SN 2017eaw counterpart (blue star) roughly 200 days before core-collapse. For comparison, we also show the locations of several SNe II progenitor stars from Smartt et al. (2015) (red circles). We also plot MIST evolutionary tracks for 9–17 M_{\odot} stars.

2011). Smith et al. (2014) claim that mass-loss rates are overestimated because they are derived from $H\alpha$, infrared, or radio luminosities assuming a homogeneous wind, and clumping can produce similar luminosities with less material. Our measurement of the SN 2017eaw progenitor star mass-loss rate makes a similar assumption (i.e., we assume a uniform wind density $\rho \sim r^{-2}$), and we recover a mass-loss rate that is similar to or larger than Galactic analogs. The level of clumping in the wind can imply a significantly lower mass-loss rate.

4 DISCUSSION

We find that the SN 2017eaw progenitor star had an initial mass close to $13^{+4}_{-2} M_{\odot}$, which agrees with the mass derived in

van Dyk et al. (2017). This quantity is mostly dependent on the luminosity of the SN 2017eaw progenitor star and thus the distance and intrinsic SED of this source. If we use the closer distance to NGC 6946 (5.7 Mpc from, e.g., Sahu et al. 2006), then the implied luminosity would be $\log(L/L_{\odot}) = 4.7 \pm 0.2$ and the initial mass would be $11^{+3}_{-2} M_{\odot}$. Overall, the SN 2017eaw progenitor star is consistent with the observed distribution of SN II progenitor stars, where it is typically found that they are RSGs in the 3400–4000 K range with luminosities below $\log(L/L_{\odot}) = 5.2$. The photometric evolution of SN 2017eaw (Tsvetkov et al. 2018), which involved a long plateau phase, and broad lines of $H\alpha$ in early-time spectra of SN 2017eaw (Figure 3 and Cheng et al. 2017) all support the conclusion that the progenitor star was a RSG with an extended hydrogen envelope.

Our preferred mass is high for a SN II progenitor system (in the upper 76th percentile of the distribution in Smartt et al. 2015). We considered the probability that all of the current sample of SN II progenitor stars with reported initial mass estimates would all have $8 M_{\odot} < M_{\text{init}} < 17 M_{\odot}$. Assuming a Salpeter initial mass function, this is a 0.26% probability for 14 sources. Although this is a relatively crude estimate of the likelihood of an upper limit on mass compared to Smartt et al. (2015) and Davies & Beasor (2018), this analysis suggests that the current sample is consistent with an upper mass limit assuming the masses are all accurate.

The evidence for circumstellar extinction around the SN 2017eaw progenitor star supports the conclusion that some progenitor mass estimates are low. In particular, the luminosities of candidate progenitor stars with only a single band of pre-explosion imaging have large systematic uncertainties (e.g., SN 2013ej; Fraser et al. 2014). We have shown that the dust shell around SN 2017eaw was compact ($4000 R_{\odot}$), and so it is likely that this dust was vaporized within the first few days after explosion. This ought to be the case if the dust was mostly produced within the last decade before explosion, which is supported by the decrease in $F814W$ and enhancement in $4.5 \mu\text{m}$ luminosity around 1000 days before discovery. Even if the light curves and spectra of SN 2017eaw (or any other SN II-P) do not appear significantly red-

dened, it is still likely that circumstellar dust played a role in reddening the pre-explosion source. This dust is more easily observed in mid-infrared bands, and so greater emphasis must be placed on obtaining imaging of SN progenitor stars beyond $2\ \mu\text{m}$.

Once SN 2017eaw fades below the magnitude of this star, it will be straightforward to image the explosion site again and verify that the source has disappeared. Deeper imaging can also be used to subtract any residual flux at the location of the progenitor and determine whether this system hosted a companion star. The majority of massive stars will exchange mass with a companion at some point during their evolution (Sana et al. 2012; de Mink et al. 2014). Furthermore, there is direct evidence that SN 1993J left a surviving companion star (e.g., Maund et al. 2004; Fox et al. 2014), but there is no such evidence for SN II-P progenitor stars. Deep, targeted follow-up of nearby core-collapse SNe is an effective way to investigate the role of binary star evolution in producing these objects.

The proximity of SN 2017eaw and its location in a galaxy with 10 luminous transients over the past hundred years presents a rare opportunity to study the environment and evolution of a SN II in detail through very late phases. Follow-up observations to study the metallicity, local environment, and any late-time circumstellar interaction around SN 2017eaw will help to resolve many lingering uncertainties in the properties of its progenitor system.

ACKNOWLEDGMENTS

We would like to thank Ori Fox and Nathan Smith for helpful discussions.

This work is supported by NSF grant AST1518052, the Gordon & Betty Moore Foundation, the Heising-Simons Foundation, and by fellowships from the Alfred P. Sloan Foundation and the David and Lucile Packard Foundation to R.J.F.

This work is based in part on observations made with the *Spitzer Space Telescope*, which is operated by the Jet Propulsion Laboratory, California Institute of Technology, under a contract with NASA. The *Hubble Space Telescope (HST)* is operated by NASA/ESA. The *HST* data used in this manuscript come from programs SNAP-9788, GO-14156, GO-14638, GO-14786, and SNAP-15166 (PIs Ho, Leroy, Long, Williams, and Filippenko, respectively). Some of our analysis is based on data obtained from the *HST* archive operated by STScI. This work makes use of observations from the LCOGT network.

Facilities: *HST* (ACS/WFC3), *Spitzer* (IRAC), LCO (FLOYDS)

REFERENCES

- Adams S. M., Kochanek C. S., Gerke J. R., Stanek K. Z., Dai X., 2017, *MNRAS*, **468**, 4968
- Barlow M. J., et al., 2005, *ApJ*, **627**, L113
- Beasar E. R., Davies B., 2016, *MNRAS*, **463**, 1269
- Braun K., Baade R., Reimers D., Hagen H.-J., 2012, *A&A*, **546**, A3
- Brown T. M., et al., 2013, *PASP*, **125**, 1031
- Bullivant C., et al., 2018, *MNRAS*, **476**, 1497
- Cheng Y.-C., Chen T.-W., Prentice S., 2017, *The Astronomer's Telegram*, **10374**
- Chevalier R. A., Fransson C., 2003, in Weiler K., ed., *Lecture Notes in Physics*, Berlin Springer Verlag Vol. 598, *Supernovae and Gamma-Ray Bursters*. pp 171–194 ([arXiv:astro-ph/0110060](https://arxiv.org/abs/astro-ph/0110060)), doi:10.1007/3-540-45863-8_10
- Choi J., Dotter A., Conroy C., Cantiello M., Paxton B., Johnson B. D., 2016, *ApJ*, **823**, 102
- Crockett R. M., Smartt S. J., Pastorello A., Eldridge J. J., Stephens A. W., Maund J. R., Mattila S., 2011, *MNRAS*, **410**, 2767
- Dall’Ora M., et al., 2014, *ApJ*, **787**, 139
- Davies B., Beasar E. R., 2018, *MNRAS*, **474**, 2116
- Decin L., Hony S., de Koter A., Justtanont K., Tielens A. G. G. M., Waters L. B. F. M., 2006, *A&A*, **456**, 549
- Dotter A., 2016, *ApJS*, **222**, 8
- Dwarkadas V. V., 2014, *MNRAS*, **440**, 1917
- Dwarkadas V. V., Gruszko J., 2012, *MNRAS*, **419**, 1515
- Elias-Rosa N., et al., 2011, *ApJ*, **742**, 6
- Epinat B., et al., 2008, *MNRAS*, **388**, 500
- Fox O. D., Chevalier R. A., Dwek E., Skrutskie M. F., Sugerman B. E. K., Leisenring J. M., 2010, *ApJ*, **725**, 1768
- Fox O. D., et al., 2011, *ApJ*, **741**, 7
- Fox O. D., et al., 2014, *ApJ*, **790**, 17
- Fraser M., et al., 2010, *ApJ*, **714**, L280
- Fraser M., et al., 2011, *MNRAS*, **417**, 1417
- Fraser M., et al., 2012, *ApJ*, **759**, L13
- Fraser M., et al., 2014, *MNRAS*, **439**, L56
- Gerke J. R., Kochanek C. S., Stanek K. Z., 2015, *MNRAS*, **450**, 3289
- Gustafsson B., Edvardsson B., Eriksson K., Jørgensen U. G., Nordlund Å., Plez B., 2008, *A&A*, **486**, 951
- Huggins P. J., Bachiller R., Cox P., Forveille T., 1994, *ApJ*, **424**, L127
- Johnson S. A., Kochanek C. S., Adams S. M., 2017, preprint, ([arXiv:1712.03957](https://arxiv.org/abs/1712.03957))
- Khazov D., et al., 2016, *ApJ*, **818**, 3
- Kilpatrick C. D., et al., 2018, *MNRAS*, **473**, 4805
- Knapp G. R., Phillips T. G., Leighton R. B., Lo K. Y., Wannier P. G., Wooten H. A., Huggins P. J., 1982, *ApJ*, **252**, 616
- Kochanek C. S., Beacom J. F., Kistler M. D., Prieto J. L., Stanek K. Z., Thompson T. A., Yüksel H., 2008, *ApJ*, **684**, 1336
- Kochanek C. S., Szczygiel D. M., Stanek K. Z., 2012, *ApJ*, **758**, 142
- Kochanek C. S., et al., 2017, *MNRAS*, **467**, 3347
- Levesque E. M., Massey P., Olsen K. A. G., Plez B., Josselin E., Maeder A., Meynet G., 2005, *ApJ*, **628**, 973
- Li W., Van Dyk S. D., Filippenko A. V., Cuillandre J.-C., 2005, *PASP*, **117**, 121
- Lovegrove E., Woosley S. E., 2013, *ApJ*, **769**, 109
- Massey P., Plez B., Levesque E. M., Olsen K. A. G., Clayton G. C., Josselin E., 2005, *ApJ*, **634**, 1286
- Massey P., Plez B., Levesque E. M., Olsen K. A. G., Silva D. R., Clayton G. C., 2009, in Luttermoser D. G., Smith B. J., Stencel R. E., eds, *Astronomical Society of the Pacific Conference Series Vol. 412, The Biggest, Baddest, Coolest Stars*. p. 3
- Mathis J. S., Rimpl W., Nordsieck K. H., 1977, *ApJ*, **217**, 425
- Maund J. R., 2009, in Giobbi G., Tornambe A., Raimondo G., Limongi M., Antonelli L. A., Menci N., Brocato E., eds, *American Institute of Physics Conference Series Vol. 1111, American Institute of Physics Conference Series*. pp 291–298, doi:10.1063/1.3141563
- Maund J. R., Smartt S. J., 2009, *Science*, **324**, 486
- Maund J. R., Smartt S. J., Kudritzki R. P., Podsiadlowski P., Gilmore G. F., 2004, *Nature*, **427**, 129
- Maund J. R., et al., 2013, *MNRAS*, **431**, L102
- Maund J. R., Reilly E., Mattila S., 2014, *MNRAS*, **438**, 938
- Mauron N., Josselin E., 2011, *A&A*, **526**, A156
- Murphy J. W., Khan R., Williams B., Dolphin A. E., Dalcanton J., Díaz-Rodríguez M., 2018, preprint, ([arXiv:1803.00024](https://arxiv.org/abs/1803.00024))
- Paxton B., Bildsten L., Dotter A., Herwig F., Lesaffre P., Timmes F., 2011, *ApJS*, **192**, 3
- Paxton B., et al., 2013, *ApJS*, **208**, 4
- Paxton B., et al., 2015, *ApJS*, **220**, 15
- Piro A. L., 2013, *ApJ*, **768**, L14
- Poznanski D., Prochaska J. X., Bloom J. S., 2012, *MNRAS*, **426**, 1465
- Prieto J. L., et al., 2008, *ApJ*, **681**, L9
- Reimers D., Hagen H.-J., Baade R., Braun K., 2008, *A&A*, **491**, 229
- Rodríguez Ó., Clocchiatti A., Hamuy M., 2014, *AJ*, **148**, 107
- Rubin A., et al., 2016, *ApJ*, **820**, 33
- Sahu D. K., Anupama G. C., Srividya S., Muneer S., 2006, *MNRAS*, **372**, 1315
- Sana H., et al., 2012, *Science*, **337**, 444
- Schlaflly E. F., Finkbeiner D. P., 2011, *ApJ*, **737**, 103
- Smartt S. J., 2009, *ARA&A*, **47**, 63

- Smartt S. J., Maund J. R., Hendry M. A., Tout C. A., Gilmore G. F., Mattila S., Benn C. R., 2004, *Science*, 303, 499
- Smartt S. J., et al., 2015, *A&A*, 579, A40
- Smith N., Li W., Filippenko A. V., Chornock R., 2011, *MNRAS*, 412, 1522
- Smith N., Mauerhan J. C., Prieto J. L., 2014, *MNRAS*, 438, 1191
- Terry J. N., Patirel G., Ekholm T., 2002, *A&A*, 393, 57
- Tikhonov N. A., 2014, *Astronomy Letters*, 40, 537
- Tinyanont S., et al., 2016, *ApJ*, 833, 231
- Tomasella L., et al., 2013, *MNRAS*, 434, 1636
- Tsvetkov D. Y., et al., 2018, preprint, ([arXiv:1801.00340](https://arxiv.org/abs/1801.00340))
- Van Dyk S. D., et al., 2012, *ApJ*, 756, 131
- Verhoelst T., van der Zypen N., Hony S., Decin L., Cami J., Eriksson K., 2009, *A&A*, 498, 127
- Walmswell J. J., Eldridge J. J., 2012, *MNRAS*, 419, 2054
- Wiggins P., 2017, Central Bureau Electronic Telegrams, 4390
- Williams B. F., Hillis T. J., Murphy J. W., Gilbert K., Dalcanton J. J., Dolphin A. E., 2018, preprint, ([arXiv:1803.08112](https://arxiv.org/abs/1803.08112))
- Woodhams M., 1993, in Cassinelli J. P., Churchwell E. B., eds, *Astronomical Society of the Pacific Conference Series Vol. 35, Massive Stars: Their Lives in the Interstellar Medium*. p. 231
- Woosley S. E., Heger A., 2012, *ApJ*, 752, 32
- de Mink S. E., Sana H., Langer N., Izzard R. G., Schneider F. R. N., 2014, *ApJ*, 782, 7
- van Dyk S. D., Filippenko A. V., Fox O. D., Kelly P. L., Milisavljevic D., Smith N., 2017, *The Astronomer's Telegram*, 10378